processes

MDPI

Article

Research on the Effect of Shale Core Mechanical Behavior on Casing Deformation

Dongfeng Li [1,2], Zhanyou He [3], Rui Wang [1,*], Le Zhang [1], Heng Fan [4], Hailiang Nie [1] and Zixiong Mo [1]

[1] CNPC Tubular Goods Research Institute, Xi'an 710077, China
[2] College of Pipeline and Civil Engineering, China University of Petroleum (East China), Qingdao 266580, China
[3] Research Institute of Oil and Gas Technology of Changqing Oilfield Company, Xi'an 710018, China
[4] School of Electronic Engineering, Xi'an Shiyou University, Xi'an 710077, China
* Correspondence: wangruitgri@163.com

Abstract: As an unconventional, high-quality, efficient, and clean low-carbon energy, shale gas has become a new bright spot in the exploration and development of global oil and gas resources. However, with the increasing development of shale gas in recent years, the anisotropic load of the shale reservoir during the mining process has caused the casing to be deformed or damaged more and more seriously. In this paper, the mechanical behavior of shale core shear, triaxial and radial compression are studied using rock true compression tests, shear tests and nuclear magnetic resonance (NMR) technology. The process of macroscopic and microscopic changes of shale fractures during the tests were analyzed to predict the effect of the fracture-state changes and stress-state changes of different shale reservoirs on the casing deformation. The results show that after the shale core is damaged, the overall pore structure changes, resulting in the decrease or increase in shale porosity. During the process of triaxial pressurization, as the pressure continues to increase, there will be a critical pressure value from elastic deformation to plastic deformation. When the pressure value exceeds the critical pressure value, the shale reservoir will have strong stress sensitivity, which can easily cause wellbore collapse. The research results have important guiding significance for determining the casing deformation under shale reservoir load and preventing casing deformation failure.

Keywords: shale; mechanical behavior; triaxial compression; stress sensitivity; casing deformation

Citation: Li, D.; He, Z.; Wang, R.; Zhang, L.; Fan, H.; Nie, H.; Mo, Z. Research on the Effect of Shale Core Mechanical Behavior on Casing Deformation. *Processes* **2023**, *11*, 274. https://doi.org/10.3390/pr11010274

Academic Editor: Qingbang Meng

Received: 14 November 2022
Revised: 31 December 2022
Accepted: 4 January 2023
Published: 14 January 2023

1. Introduction

As an unconventional, high-quality, high-efficiency, and clean low-carbon energy, shale gas can form a benign complement to other low-emission energy sources such as nuclear energy and renewable energy, and it is the most realistic choice for a clean energy supply. Since the outbreak of the shale gas revolution in the United States and the successful large-scale commercial exploitation of shale gas, the exploration and development of unconventional oil and gas resources led by shale gas has attracted great attention from all over the world [1–3].

However, with the increasing development of shale gas in recent years, the deformation or damage of casing has become more and more serious [4–6]. Research on casing damage mechanisms are mainly aimed at research on casing damage mechanisms caused by over-exploitation of shale reservoirs [7–9]. The collapse and bending of casing usually occur in the central area of the gas reservoir with high mud content and water content, and the shearing and bending occur in the overlying strata at the edge of the gas reservoir. It is considered that the mechanism of casing damage is the discontinuous deformation of the overlying strata. These discontinuous deformations include subsidence-induced interlayer slip and fault movement resulting in casing shear damage. The axial compression and bending of the casing are caused by large vertical displacements. When the pore pressure drops and the gas layer is compacted, the axial load is transferred from the stratum to the cement sheath, and then transferred to the casing. As a result, the casing is damaged

due to yielding or bending failure. In the middle of the production layer, the casing is collapsed and damaged, when the axial strain is the largest, the casing is unstable and bent due to the excessive axial load and insufficient lateral support around it, which lead to the deformation of the casing in the wellbore.

The main reason for this in China is that in the process of hydraulic fracturing, the fracturing fluid exceeds the fracture pressure in the case of poor cementing quality, and a large amount of fracturing fluid enters the stratum form a communication channel and causes channeling [10–12]. This is because the stratum stress is out of balance and the large immersion water areas are easy to form casing damage areas. Mudstone expansion is also one of the reasons for casing damage [13,14]. It is believed that the first reason for casing damage mechanisms is that the mudstone creeps and expands and squeezes the casing under a certain external force, which often results in single-well casing damage [15]. The longitudinal distribution of the casing damage layers are dominated by the argillaceous rock layers in the gas layers and shallow gas layers. The second reason is that under the action of the block pressure difference or the topographic pressure, the difference caused by the formation dip, the strata slide in pieces and shear the casing, which often results in piece-casing damage [5,16,17]. Third, inside and outside of the development block, often due to uneven pore pressure, uneven distribution of high-pressure areas and low-pressure areas are formed. The expansion of the pore skeleton in the high-pressure areas causes the surrounding rock mass to rise under pressure, but in the low-pressure areas, the surrounding rock mass sinks due to the contraction of the pore skeleton [18]. The vertical lifting of this kind of rock mass can easily cause the casing to be broken. Fourth, hydraulic fracturing injects water-based fracturing fluid to hold pressure on both sides of the fault, causing the formation pressure on both sides of the fault to lose balance [19].

The above conclusions represent the current understanding of casing damage mechanisms. On the basis of the above research results, RTR-1000 rock true triaxial mechanical test equipment and shearing equipment, and NRM-200 NMR international advanced test equipment were used in this paper to evaluate the mechanical properties of shale cores in a shale gas field block, and the changes in mechanical properties before and after radial compression as well as the changes in mechanical properties in different states after shear failure. The macroscopic and microscopic states of shale fractures under different axial and radial stress states were explored using NMR. In this way, the effect of fracture-state change and stress-state change of different shale reservoirs on the casing deformation can be predicted.

2. Test Materials

In order to ensure that the research results were more consistent with the actual engineering, the test materials were taken from shale cores of an oil and gas field block in China (as shown in Figure 1). The depth of the horizon was 2188~4131 m, which belongs to marine accumulation.

Figure 1. On-site sampling photos.

3. Test Design

The shale reservoir cores tests included 20 groups of shear tests (specimen No 4,5,6,7-1, 7-2,12,13,18,21-1,21-2,25,26-1,26-2,27,29-1,29-2,30,33,39,42), 12 groups of triaxial compres-

sion and NMR tests (specimen No 1,2,3,4,5,6,7,8,9,10,11,12), and radial compression and NMR tests (specimen No 5-2, 6-2, 11-1, 17-1, 18-2, 23-2).

The mechanical tests in this paper mainly adopted the RTR-1000 rock true triaxial mechanical test equipment (The manufacturer is monitor instrument Co., Ltd. and the supplier is Shenzhen monitor instrument Co., Ltd. Shenzhen, China) and RecCore-2513DHNMR test equipment (The manufacturer and supplier is research institute of petroleum exploration and & development), as shown in Figure 2. The maximum axial pressure was 1000 KN, the maximum confining pressure was 140 MPa, and the pore pressure was 140 MPa. The test precision of pressure was 0.01 MPa, liquid volume was 0.01 g/cm^3, and the deformation was 0.001 mm.

(**a**) (**b**)

Figure 2. Test equipment. (**a**) RTR-1000 rock true triaxial mechanics test equipment, (**b**) RecCore-2513DHNMR test equipment.

According to the geological characteristics of the samples and the requirements of the actual test items, the samples were classified and pre-processed shown in Figure 3, mainly including sample data collection, drilling, cutting, liquid nitrogen sample preparation, etc., to ensure the accuracy of the later test analyses.

Figure 3. Shale core samples for shear test.

The sample was a cylinder of Φ25 × 50mm, the height-diameter ratio was 2.0–2.5. The diameter error along the entire height of the sample was less than 0.3 mm. The error of the non-parallelism of the two ends less was than 0.05 mm, and the error of the unevenness of the end surface was less than 0.02 mm.

4. Mechanical Test Results

4.1. Shear Test Results

Shear tests were carried out on 20 pieces of shale cores, and the normal load and horizontal shear force were controlled using displacement until the samples were sheared. The control program automatically collected the load, stress, displacement, and other values.

The shear test results are shown in Figures 4–6. It can be seen that the shear force of the shale was mainly distributed between 3.59 and 10.87 kN, and the average shear force was 7.96kN. The shear strength was mainly distributed in the range of 7.20 to 21.81 MPa, and the average shear strength was 16 kN. It can be seen from Figure 4 that the distribution

range of shear force was 15% less than 5.0 kN, 70% from 5.0 kN to 10.0 kN, and 15% more than 10.0 kN. From Figure 5, it can be concluded that the distribution range of shale shear strength was 15% less than 10.0 MPa, 70% from 10.0 MPa to 20.0 MPa, 15% more than 20.0 MPa, and the correlation between shear force and shear strength was 0.9825. The correlation was relatively good, as shown in Figure 6, which proves that within a certain range, the shear force is proportional to the shear strength.

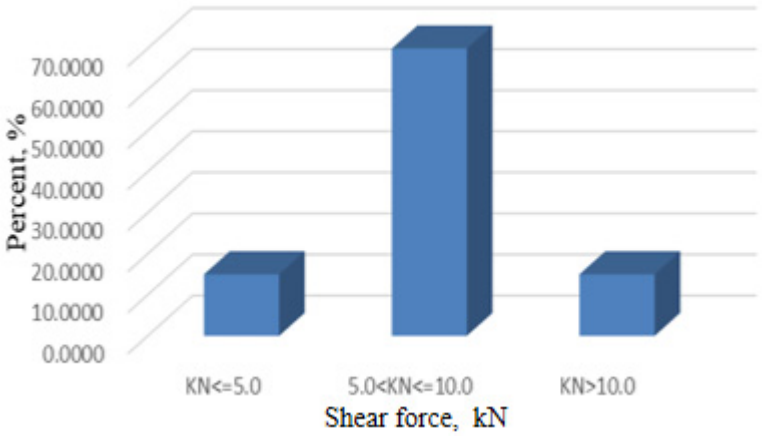

Figure 4. Frequency histogram of shear force range.

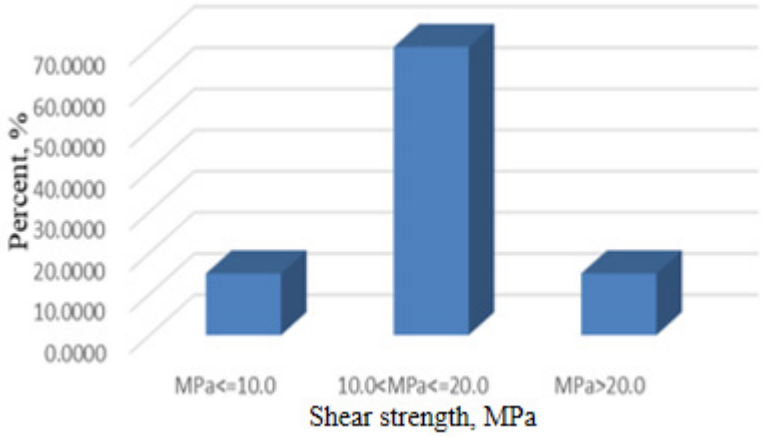

Figure 5. Frequency histogram of shear strength range.

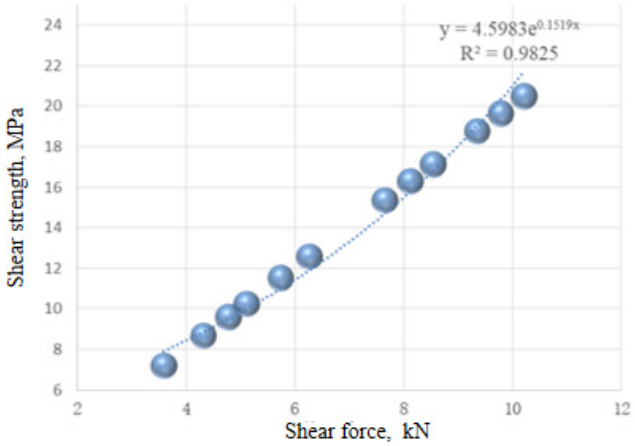

Figure 6. Correlation distribution of shear force and shear strength.

4.2. Triaxial Compression Test

The triaxial compression test was carried out on 12 pieces of shale cores. The stress and strain variation with time, triaxial compressive stress-strain curve, Young's modulus, and Poisson's ratio variation curve of 12 shale cores were obtained. Typical test results are shown in Figures 7–10.

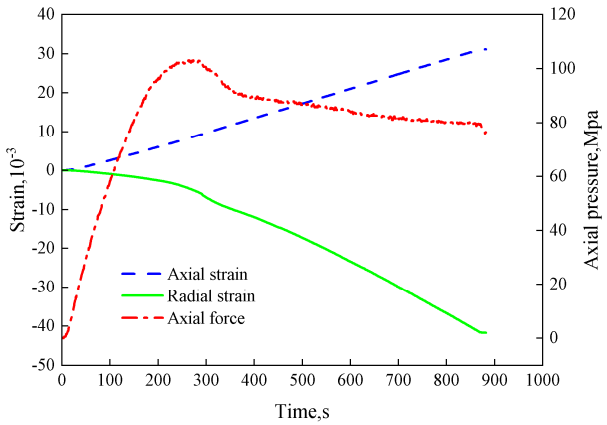

Figure 7. Typical core stress and strain time change curve.

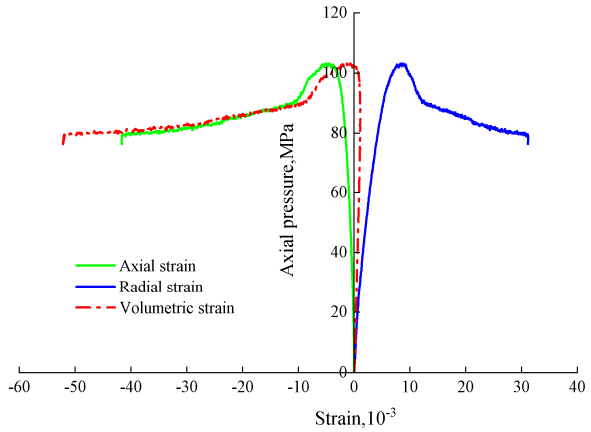

Figure 8. Typical core stress–strain curve.

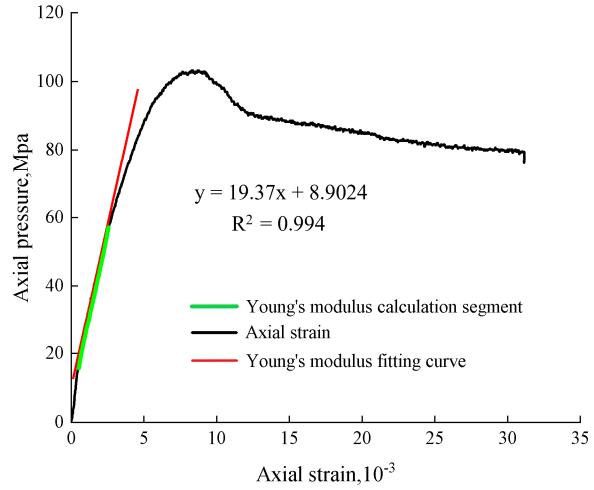

Figure 9. Variation curve of Young's modulus of typical core.

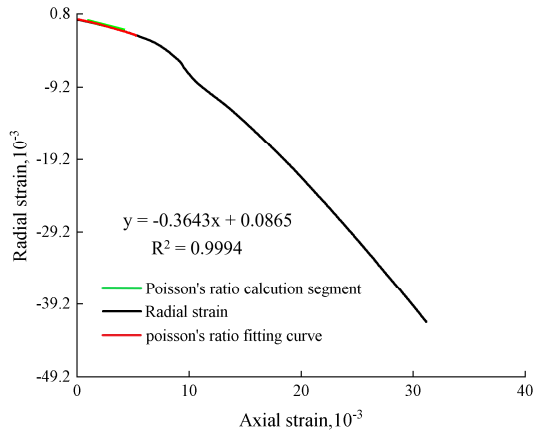

Figure 10. Variation curve of Poisson's ratio of typical cores.

Figure 11 shows the peak pressure of triaxial compression of 12 groups of core samples. The analysis data showed that the maximum compressive strength of the shale was mainly distributed in the range of 94.9 to 302.4 MPa.

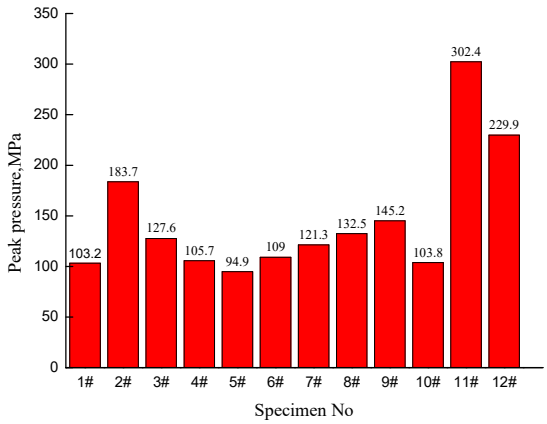

Figure 11. Distribution of peak pressure in 12 groups of core tests.

The data obtained from the 12 groups of tests were processed and analyzed to obtain the correlation distribution diagram of Young's modulus, as shown in Figures 12 and 13. It can be seen from Figure 12 that the correlation between the dynamic Young's modulus and the dynamic bulk modulus of the shale was 0.6105, and the correlation was general. The correlation was 0.6819, the distribution was relatively discrete, and its correlation was also general.

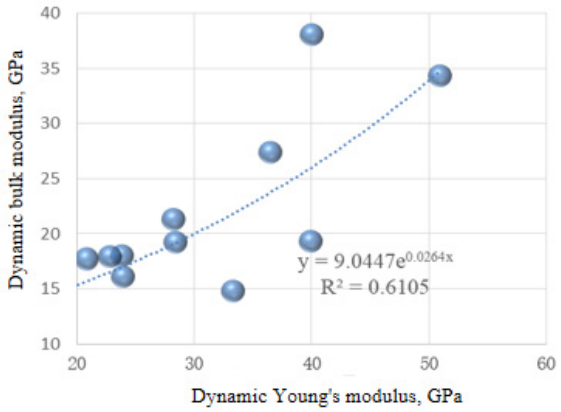

Figure 12. Distribution histogram of dynamic Young's modulus and bulk modulus.

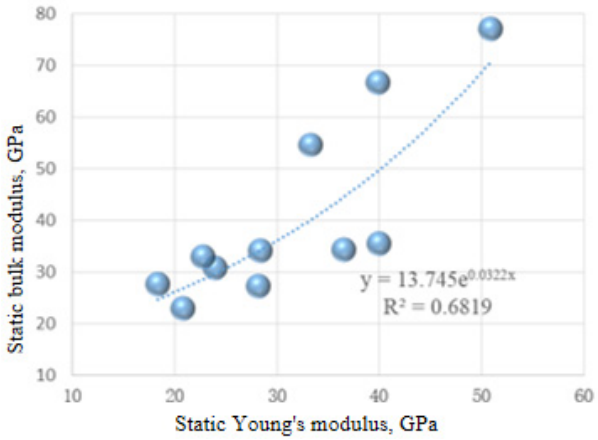

Figure 13. Histogram of the correlation distribution between static Young's modulus and bulk modulus.

4.3. Shale Radial Compression Test

Through the comparative NMR test of six pieces of shale before and after radial compression, the stress-compression curve and the elastic index change curve under different stress changes were obtained. The typical curve is shown in Figures 14 and 15.

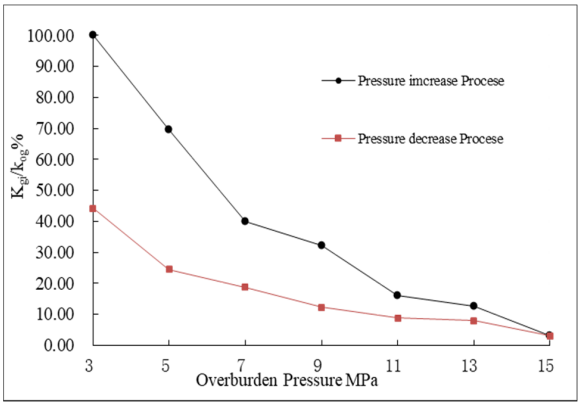

Figure 14. Typical core stress compression curve.

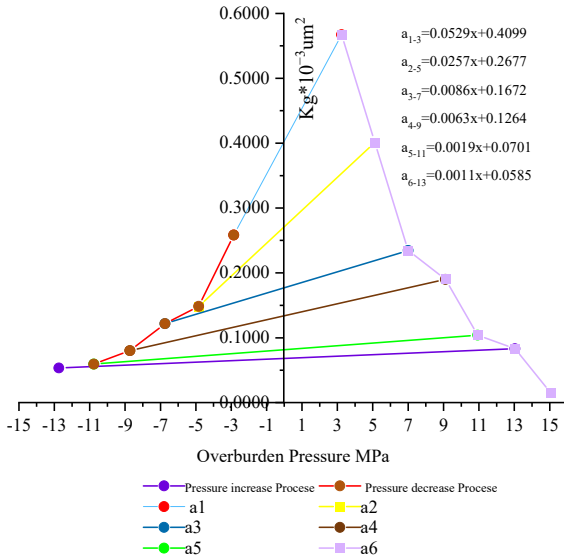

Figure 15. Curve of elastic index variation of a typical core under different stress changes.

Through data processing, the correlation distribution between radial compression force and elastic index of the shale core was obtained, as shown in Figure 16. The core elastic index decreased with the increase in radial compression force, and the correlation between the elastic index and the radial compression force was 0.9861, which is a good correlation. It showed that with the increase in radial three-axis compressive force, the core went from elastic deformation to plastic deformation.

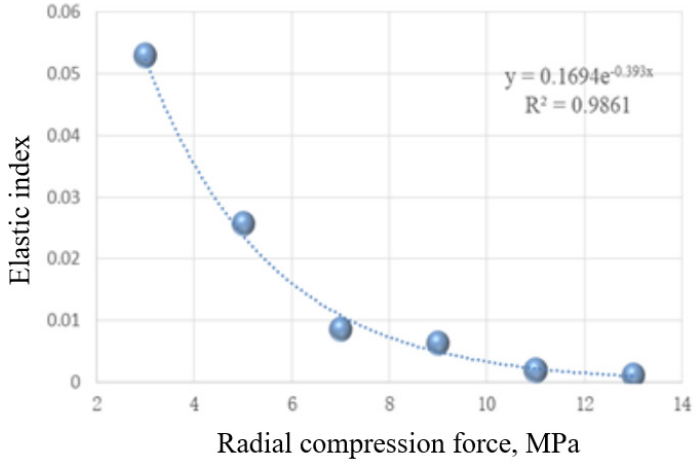

Figure 16. Correlation distribution of radial compression force and elastic index of core.

5. NMR Test and Discussion

The measurement of the porosity of the sample mainly uses the one-dimensional steady state Darcy's law. The rock sample was installed in the core holder to simulate the stress condition of the formation, and nitrogen gas was introduced to measure the gas permeability of the rock sample. The rock sample was placed in a closed saturated container, vacuumized at −0.1MPa for more than 5 h, saturated liquid was then put into the rock sample cup in the container, and then continued to vacuum until no bubbles were released. The high-pressure pump was used to simulate the formation pressure which was set for more than 24 h. The weight of the sample after saturation with the liquid and the weight of the sample in the liquid were measured. The porosity and pore volume of the sample were calculated as follows [20,21]:

$$\phi = \frac{M_1 - M_0}{M_1 - M_2} \times 100\% \quad (1)$$

$$V_\phi = \frac{M_1 - M_0}{D} \quad (2)$$

here:

ϕ—porosity;
V_ϕ—pore volume;
$M0$—the weight of the rock sample after drying, g;
$M1$—the weight of the rock sample after saturated with liquid, g;
$M2$—weight of rock sample in saturated liquid, g;
D—density of saturated liquid, g/cm^3.

The crack changes of the specimens were mainly measured using NMR tests. The prepared rock sample was placed in the NMR sample chamber, and the H nuclear energy level transition was excited by magnetizing the sample fluid, data and images were automatically collected, the T2 spectrum was fitted, and the microscopic pore structure and microfracture changes were analyzed.

5.1. NMR Test Model before and after Triaxial Compression

Comparative NMR tests were carried out on 11 groups of shale blocks before and after triaxial compression. The photos of the samples after compression are shown in Figure 17.

(**a**) (**b**)

Figure 17. Shale sample after triaxial compression. (**a**) Shale sample, (**b**) cross section of shale sample.

The typical results of NMR T2 obtained before and after triaxial compression are shown in Figure 18. Through data analysis, the frequency histogram of the degree of change in pores and cracks is shown in Figure 19.

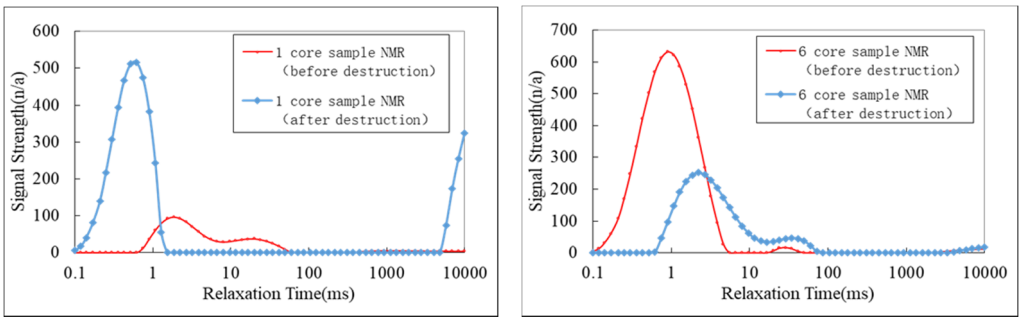

(**a**) (**b**)

Figure 18. Typical T2 spectra of cores before and after triaxial compression. (**a**) Sample 1, (**b**) sample 6.

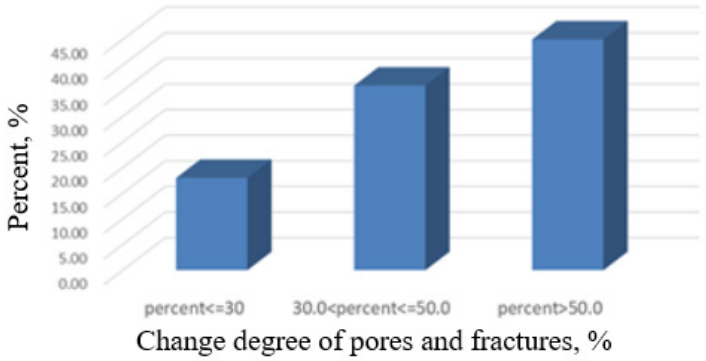

Figure 19. Frequency histogram of change degree of pores and fractures.

By studying the NMR scan results of 11 groups of shale before and after the failure, it was found that the pore and fracture amplitudes of the cores changed after the failure, and the porosity decreased or increased. This is due to the formation of micro-cracks or large cracks, which increases the change amplitude of pores and cracks. However, under the

action of triaxial radial pressure, due to the influence of clay minerals, the original microfractures may also be compressed, which reduces the variation amplitude of pores and fractures. It can be seen from Figure 19 that the distribution range of the change amplitude of pores and fractures was 18% when the change amplitude of pores and fractures was less than 30%, 36% when the change amplitude of pores and fractures was between 30 and 50%. Amplitude greater than 50% is 45%. This shows that the change amplitudes of pores and fractures before and after the failure changed greatly, which is due to the change of the amplitude of the porosity in the core before and after the failure.

5.2. Radial Compression NMR Test Model

Comparative NMR tests were carried out on six groups of shale blocks before and after triaxial compression, and the radial compression NMR T2 spectrum and the curve of the total signal value of the core with radial pressure were obtained. The typical spectrum is shown in Figure 20.

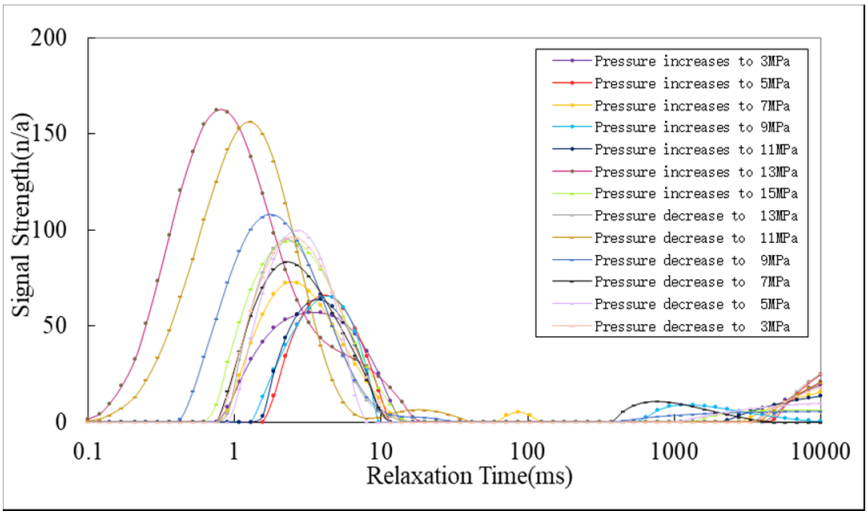

(**a**)

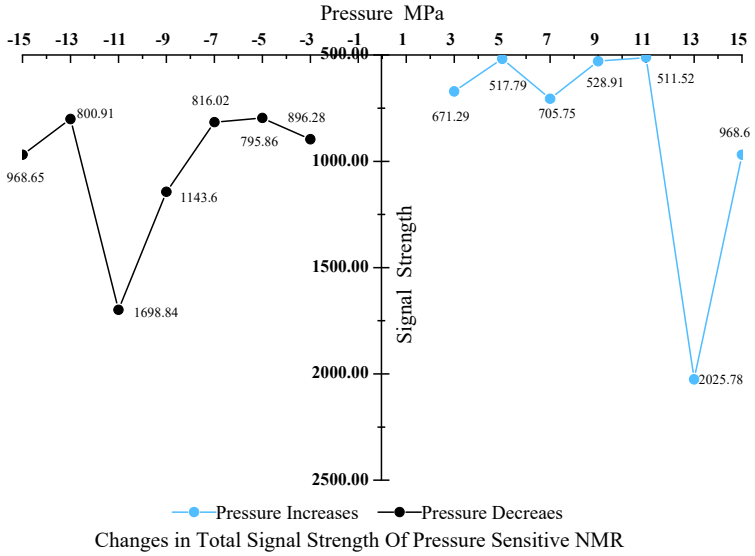

(**b**)

Figure 20. Typical radial compression NMR test spectrum. (**a**) NMR T2 spectrum, (**b**) curve of total core signal value versus radial pressure.

From the analysis of the NMR test data, it can be seen that the pore structure of the shale was also changed during the triaxial compression process. The critical pressure values of cores 5-2, 6-2, 11-1, 17-1, 18-2, and 23-2 from elastic deformation to plastic deformation were 9, 7, 5, 9, 9, and 7 MPa, respectively. When the stress increases to exceed the critical pressure value, the core will be squeezed to form micro-cracks. Continued pressurization will cause the mineral particles and clay inside the core to squeeze each other to block the cracks and reduce the core porosity. The recovery process is the competitive recovery of fractures and pores, so the amplitudes of core pores and fractures will vary.

Figure 21 is a typical curve of the free water signal changing with the radial compressive stress. The change curve of the free water content in the shale with the radial confining pressure can be obtained from the map analysis. Generally speaking, the higher the free water content in the core, the higher the irreducible water content. The lower the content, the less shale content in the shale.

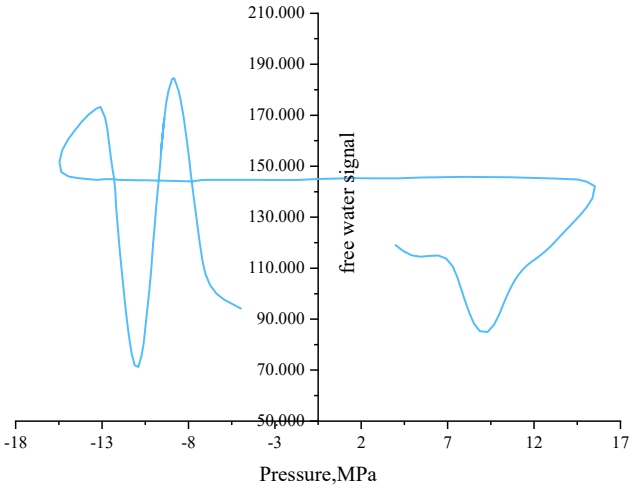

Figure 21. Core free water signal and radial compressive stress curve.

Table 1 shows the change amplitudes of pores and fractures when the core is pressurized and decompressed under the same stress. When the amplitude change was the largest, it showed that the pores and fractures in the shale changed greatly and with the increase in stress. Within a certain range, the change amplitude of pores and fractures also increased, indicating that the greater the compressive stress, the greater the impact on the shale pore structure; however, when the stress reached a certain large value, the shale underwent plastic deformation, and the change of the pore and fracture amplitude was relatively small.

Table 1. Variation amplitude of pores and fractures in cores under pressure and decompression under the same stress.

Radial Pressure, MPa	The Variation Amplitude of Pores and Fractures When the Core is Pressurized and Decompressed under the Same Stress, %					
	No. 5-2	**No. 6-2**	**No. 11-1**	**No. 17-1**	**No.18-2**	**No.23-2**
3-(-3)	25.10	22.27	12.80	20.02	41.47	43.24
5-(-5)	34.94	18.00	21.64	2.32	15.35	36.59
7-(-7)	13.51	33.95	25.70	20.41	16.24	34.39
9-(-9)	53.75	19.81	2.81	18.82	29.80	23.91
11-(-11)	69.89	48.82	38.67	45.46	42.90	47.70
13-(-13)	60.46	1.12	10.22	46.66	46.34	4.36

Table 2 shows the variation amplitudes of pores and fractures in the process of core pressurization and decompression. When the amplitude changes were the largest, the pores

and fractures in the shale changed greatly, which is the process of the core from elastic deformation to plastic deformation. From the analysis of the table, it can be concluded that the fracture pressure range of the shale wall is 11–13 MPa for the No. 5-2 core, 13–11 MPa for the No. 6-2 core, 11–9 MPa for the No. 11-1 core, and 17-1 for the No. 17-1 core. The core is 11–13 MPa, the No. 18-2 core is 11–13 MPa, and the No. 23-2 core is 9–11 MPa. This provides a reliable basis for studying the microscopic mechanism of casing damage deformation and preventing casing damage.

Table 2. The data table of the change amplitude of pores and fractures in the core during the pressurization and decompression process.

Radial Pressure, MPa	The Variation Amplitude of Pores and Fractures in the Core Pressurization and Decompression Process, %					
	No. 5-2	No. 6-2	No. 11-1	No. 17-1	No. 18-2	No. 23-2
3-5	22.87	8.30	3.00	19.18	28.04	7.57
5-7	26.63	1.35	2.09	28.81	14.07	7.90
7-9	25.06	5.20	7.72	5.96	7.12	1.08
9-11	3.29	1.70	8.24	7.45	18.25	65.30
11-13	74.75	0.70	4.63	61.96	48.26	54.55
13-15	52.18	0.18	2.23	29.62	42.51	10.65
15-13	17.32	0.94	12.22	24.21	6.65	6.58
13-11	52.86	47.88	28.37	23.51	40.77	16.88
11-9	32.68	37.26	31.23	27.41	33.49	12.78
9-7	28.64	21.92	17.16	4.08	9.77	12.83
7-5	2.47	20.54	7.16	8.43	13.15	4.70
5-3	11.20	3.26	7.36	3.33	3.93	17.25

Using the NMR test system, the pore structure, permeability, and other physical/mecha nical property parameters of shale-rock fractures were monitored in real time. The test results provided the original data for the finite element method to simulate the casing deformation under formation-slip conditions.

6. The Effect of Shale Core Mechanical Behavior on Casing Deformation

Taking a shale gas well as an example, the well was 418.4 m above sea level, the calculated position was 2173–4122 m, the production casing steel grade was Q125, the diameter was 127 mm, and the wall thickness was 12.14 mm. Through tensile test, the yield strength of casing was 984 MPa, the ultimate strength was 1049 MPa, and the strain was 0.0647. The elastic modulus of shale was 19.34 GPa, and the ultimate compressive strength was between 94.9 and 302.4 MPa. The input parameters of finite element model was shown in Table 3.

Table 3. The input parameters of finite element model.

Parameter	Model		
	Casing	Cement Ring	Rock Layer
Modulus of elasticity/GPa	210	12	19.34
Poisson ratio	0.25	0.20	0.20
Yield strength/MPa	984	30	40

According to the logging data, the main failure mode of the casing in this well was shear failure, and the formation slip was between 0.8 and 10.2 mm. Therefore, the finite element calculation model as shown in Figure 22 was established, and the formation slip amounts of 2, 4, 6, 8, and 10 mm were applied to obtain the formation casings with shale compressive strengths of 100, 150, 200, 250, and 300 MPa, respectively. Stress and deformation results of the coupled model.

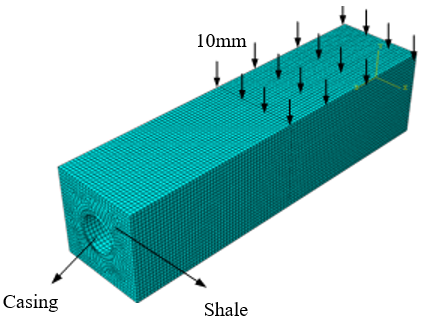

Figure 22. Mesh diagram of finite element analysis.

Figure 23a–e are the Mises stress nephograms of the casing under the rock compressive strength of 100, 150, 200, 250, and 300 MPa, and the maximum slip of the formation was 10 mm. Figure 24 shows the mises stress of the casing along the axial direction of the casing. It can be seen from the Figure that under this condition, the casing reached its ultimate strength of 1049 MPa. The main deformation position was about 20 mm in length at the shear slip of the rock stratum.

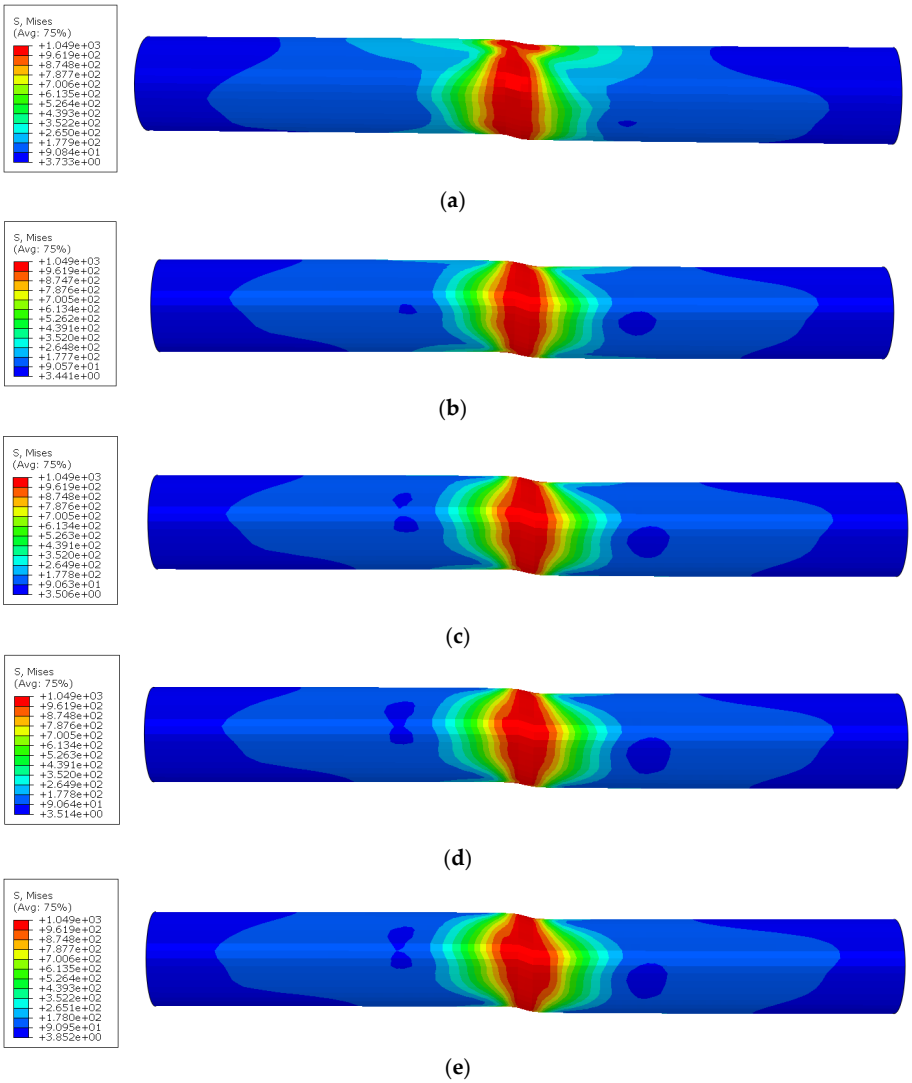

Figure 23. Cloud map of finite element calculation results. (**a**) Rock compressive strength 100 MPa, (**b**) rock compressive strength 150 MPa, (**c**) rock compressive strength 200 MPa, (**d**) rock compressive strength 250 MPa, (**e**) rock compressive strength 300 MPa.

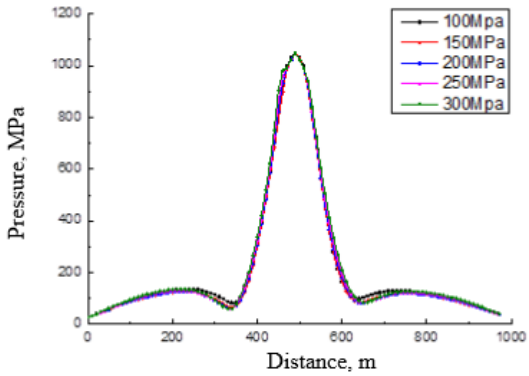

Figure 24. Variation curve of casing stress along the axial direction of different rock compressive strengths when the slip is 10 mm.

Figure 25 shows the slippage of the rock formation when the casing reaches the ultimate anti-deformation capacity under different rock compressive strengths; under the slippage of 10 mm, the deformation of the casing at the maximum stress position of the casing. It can be seen that when the rock layer slipped by about 4.5 mm, the casing had reached the ultimate bearing capacity, and its ultimate deformation resistance gradually decreased with the increase in the shale compressive capacity. However, under 10 mm slippage, with the increase in rock compressive strength, the deformation of casing decreased slightly and remained basically the same.

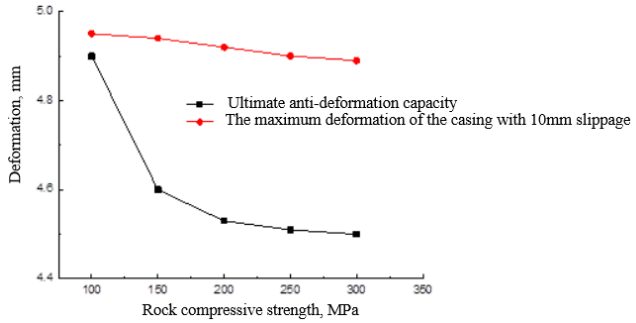

Figure 25. Curve of casing deformation resistance under different rock compressive strengths.

7. Conclusions

In this paper, the triaxial compression, shearing, radial compression force, and critical yield force tests were carried out on the shale. Combined with NMR technology, we mastered the shale fracture expansion and change laws, and the original pore structure, and it provides a reliable basis for preventing casing damage.

The critical compressive strength and maximum shear strength of the reservoir under different stresses can be obtained from the triaxial compression and direct shear tests. The compressive strength of shale was found to be 94.9–302.4 MPa, and the shear strength was 7.20–21.81 MPa. This provides a basis for studying the microscopic mechanism of casing damage. After the core was damaged, the overall pore structure changed, and the most of the changes in pores and fractures were more than 30%, which resulted in a decrease or increase in shale porosity. NMR tests showed that in the process of triaxial pressurization, the critical pressure value from elastic deformation to plastic deformation appeared as the pressure continued to increase. When the triaxial stress exceeds the critical pressure value, micro-fractures will be formed in clay or organic matter, and at the same time, clay particles will deform to block other pores or fractures, making shale reservoirs highly sensitive to stress and easily leading to wellbore collapse. The shale fracture wellbore collapse pressure range studied in this paper was 9–13 MPa. The above data provide a reliable basis for studying the microscopic mechanism of casing damage and preventing casing damage.

Through the analysis of casing stress and deformation under different rock compressive strengths and without rock slip, it is shown that the smaller the rock compressive strength, the better the protective effect on casing. Therefore, the method of reducing the strength of cement sheath can be adopted to prevent casing deformation.

Author Contributions: Conceptualization, D.L. and Z.H.; methodology, R.W.; software, H.F.; validation, L.Z., H.N. and Z.M.; formal analysis, D.L.; investigation, R.W.; resources, L.Z.; data curation, H.F.; writing—original draft preparation, D.L. and R.W.; writing—review and editing, R.W.; visualization, L.Z., H.N. and Z.M.; supervision, Z.H. and H.F.; project administration, D.L.; funding acquisition, D.L. All authors have read and agreed to the published version of the manuscript.

Funding: This research was funded by CNPC R&D project "Research and development of new casing to improve casing damage resistance of shale gas wells" (2020B-4020).

Data Availability Statement: Not applicable.

Conflicts of Interest: The authors declare no conflict of interest.

References

1. Wang, Q.; Chen, X.; Jha, A.N. Howard Rogers. Natural gas from shale formation—The evolution, evidences and challenges of shale gas revolution in United States. *Renew. Sustain. Energy Rev.* **2014**, *30*, 1–28. [CrossRef]
2. Song, W.; Chang, Y.; Liu, X.; Li, K.; Gong, Y.; He, G.; Wang, X.; Christie, P.; Zheng, M.; Dore, A.J.; et al. A Multiyear Assessment of Air Quality Benefits from China's Emerging Shale Gas Revolution: Urumqi as a Case Study. *Environ. Sci. Technol.* **2015**, *49*, 2066–2072. [CrossRef] [PubMed]
3. Geng, J.-B.; Ji, Q.; Fan, Y. The impact of the North American shale gas revolution on regional natural gas markets: Evidence from the regime-switching model. *Energy Policy* **2016**, *96*, 167–178. [CrossRef]
4. Hu, C.; Ai, C.; Tao, F.; Wang, F.; Yan, M. Optimization of Well Completion Method and Casing Design Parameters to Delay Casing Impairment Caused by Formation Slippage. In Proceedings of the SPE/IADC Middle East Drilling Technology Conference and Exhibition, Abu Dhabi, United Arab Emirates, 26–28 January 2016.
5. Yan, W.; Zou, L.; Li, H.; Deng, J.; Ge, H.; Wang, H. Investigation of casing deformation during hydraulic fracturing in high geo-stress shale gas play. *J. Pet. Sci. Eng.* **2017**, *150*, 22–29. [CrossRef]
6. Tian, Z.; Shi, L.; Qiao, L. Problems in the wellbore integrity of a shale gas horizontal well and corresponding countermeasures. *Nat. Gas Ind. B* **2015**, *2*, 522–529. [CrossRef]
7. Lyu, Q.; Ranjith, P.; Long, X.; Kang, Y.; Huang, M. A review of shale swelling by water adsorption. *J. Nat. Gas Sci. Eng.* **2015**, *27*, 1421–1431. [CrossRef]
8. Li, Z.; Li, H.; Li, G.; Yu, H.; Jiang, Z.; Liu, H.; Hu, S.; Tang, B. The influence of shale swelling on casing deformation during hydraulic fracturing. *J. Pet. Sci. Eng.* **2021**, *205*, 108844. [CrossRef]
9. Xiumei, L.V.; Liu, J.; Pei, J. Effect Analysis of Water Invading Shale Expansion on Casingdamage. In Proceedings of the International Symposium on Multi-Field Coupling Theory of Rock and Soil Media and Its Applications, Chengdu, China, 10–12 October 2010; Logging & Testing Services Company of Daqing Oilfield Co., Ltd.: Daqing, China, 2010.
10. Li, H.; Li, Z.; Li, G.; Yu, H.; Jiang, Z.; He, L.; Guo, B.; Dong, M. Casing deformation mechanisms of horizontal wells in Weirong shale gas field during multistage hydraulic fracturing. *J. Nat. Gas Sci. Eng.* **2020**, *84*, 103646. [CrossRef]
11. Lin, H.; Mao, L.; Mai, Y. Influence of multistage fracturing in shale gas wells on the casing deformation of horizontal wells. *Pet. Sci. Technol.* **2022**, 1–25. [CrossRef]
12. Chen, D.; Pan, Z.; Ye, Z. Dependence of gas shale fracture permeability on effective stress and reservoir pressure: Model match and insights. *Fuel* **2015**, *139*, 383–392. [CrossRef]
13. Du, J.; Hu, L.; Meegoda, J.N.; Zhang, G. Shale softening: Observations, phenomenological behavior, and mechanisms. *Appl. Clay Sci.* **2018**, *161*, 290–300. [CrossRef]
14. Chen, Z.; Lin, S.; Xiang, D. Mechanism of casing deformation in the Changning–Weiyuan national shale gas demonstration area and countermeasures. *Nat. Gas Ind. B* **2017**, *4*, 1–6. [CrossRef]
15. Li, L.; Wang, G.; Lian, Z.; Zhang, L.; Mei, J.; He, Y. Deformation mechanism of horizontal shale gas well production casing and its engineering solution: A case study on the Huangjinba Block of the Zhaotong National Shale Gas Demonstration Zone. *Nat. Gas Ind. B* **2018**, *5*, 261–269. [CrossRef]
16. Yin, F.; Xiao, Y.; Han, L.; Wu, X. Quantifying the induced fracture slip and casing deformation in hydraulically fracturing shale gas wells. *J. Nat. Gas Sci. Eng.* **2018**, *60*, 103–111. [CrossRef]
17. Fei, Y.; Han, L.; Yang, S.; Deng, Y.; He, Y.; Wu, X. Casing deformation from fracture slip in hydraulic fracturing. *J. Pet. Sci. Eng.* **2018**, *166*, 235–241.
18. Eveline, V.F.; Akkutlu, I.Y. Osmosis and Clay Swelling Effects in Gas Shale Formations under Stress. In Proceedings of the SPE Annual Technical Conference and Exhibition, Dallas, TX, USA, 24–26 September 2018.

19. Zhou, Z.; Abass, H.; Li, X.; Bearinger, D.; Frank, W. Mechanisms of imbibition during hydraulic fracturing in shale formations. *J. Pet. Sci. Eng.* **2016**, *141*, 125–132. [CrossRef]
20. Sondergeld, C.H.; Newsham, K.E.; Comisky, J.T.; Rice, M.C. Petrophysical Considerations in Evaluating and Producing Shale Gas Resources. In Proceedings of the SPE Unconventional Gas Conference, Pittsburgh, PA, USA, 23–25 February 2010.
21. Li, x.; Zhou, c.; Li, c.; Cheng, x.; Hu, s. Adbances in petrophysical Analysis Technology of Shale Gas. *Well Logging Technol.* **2013**, *37*, 352–359.